

GRAPHICAL PROCESSING UNIT BASED LATTICE BOLTZMANN MODELING OF CONTROL
OF A SEPARATED FLOW

by

Xuan Shi

A research proposal submitted in conformity with the requirements
for the degree of Master of Engineering
Graduate Department of Mechanical and Industrial Engineering
University of Toronto

2020 September

Abstract

Graphical Processing Unit Based Lattice Boltzmann modeling of control of a Separated Flow

Xuan Shi

Master of Engineering

Graduate Department of Mechanical and Industrial Engineering

University of Toronto

2019

A synthetic jet actuator is a zero-net-mass-flux device that imparts momentum and is useful for active flow control (AFC). To study synthetic jet performance, this paper presents model examines a synthetic jet actuator operating in a cross-flow and for a separated flow. Using a 3-D Lattice Boltzmann method (LBM) with the Bhatnagar-Gross-Krook (BGK) collision models, the effect of the SJA is shown. This work was implemented on a General Purpose Graphical Processing Unit (GP-GPU) cluster for accelerated solution. Time-dependent synthetic jet simulations were carried out for a synthetic jet actuator (SJA) operating in a cross flow and within a separation. The results show the influence of the SJA on the cross-flow pressure and momentum and the spatial limits of the control.

Acknowledgements

This work was supported by the Natural Science and Engineering Research Council of Canada and the Southern Ontario Smart Computing Innovation Platform. Computations were performed on the SOSCIP GPU cluster at the SciNet High Performance Computing consortium, which included support from the Canada Foundation for Innovation under the auspices of Compute Canada, the Government of Ontario, the Ontario Research Fund—Research Excellence, and the University of Toronto.

Contents

1	Introduction	1
2	Numerical Method and Model	4
2.1	Lattice Boltzmann Model	4
2.2	GPU implementation	6
3	Computational Domain	9
4	Results and Discussions	11
4.1	GPU performance	11
4.2	Flow from nozzle	11
4.3	Flow development in x-z plane	13
4.4	Flow development in x-y plane	14
4.5	Separated flow	17
5	Conclusions	20
	Bibliography	20

Chapter 1

Introduction

A synthetic jet transfers linear momentum to the surroundings by alternately ingesting and expelling fluid from a cavity containing an oscillating diaphragm and has been shown to be a useful AFC device [1, 2]. Compared with continuous jets, synthetic jets are low-weight, compact and do not require internal fluid supply lines [3, 4]. A schematic diagram of a typical synthetic jet actuator is shown in Fig. 1.1, which also illustrates the primary structure and shows vortex pairs emanating from a nozzle while the SJA is in operation.

A synthetic jet actuator typically has a nozzle or slot connected to a cavity in which a piezoelectric membrane oscillates. By oscillating the diaphragm, the working fluid is alternately ingested and expelled through the nozzle exit, forming a train of discrete vortical structures that impart linear momentum to the flow without net mass injection [5]. The ability of the vortex pairs to overcome the suction velocity during the ingestion stroke depends on its self-induced velocity, which in turn is a function of the vortex strength. The fact that no external fluid source is required combined with the availability of increasingly small vibrating diaphragms, e.g. piezo-electric disks, allows the design of extremely compact devices, even down to MEMS scales [6, 7].

Recently, the influence of cavity shape on synthetic jet performance has been studied with numerical simulation or experiment. Bhapkar et al. [8] conducted an experimental study to investigate the effect of orifice cavity shape on resonance frequency and heat transfer characteristics of synthetic jets. The velocity measurement results showed that the resonance frequency was a weak function of cavity volume as the resonance frequency remains. Utturkar et al. [9] employed an incompressible flow model to study the flow in rectangular cavities where the aspect ratio and location of the oscillating diaphragm was varied. Cavities containing multiple oscillating diaphragms were also considered, where the oscillation amplitude was adjusted in order to maintain the same volume displacement in each case. The paper found that cavity shape and diaphragm placement had negligible impact on the actuator performance in both quiescent conditions or with cross-flow. Jain et al. [10] provided a detailed compressible simulation of an axisymmetric synthetic jet compared with the existing experimental and numerical results for the purpose of validation. A vibrating diaphragm was simulated as a moving boundary and was compared with other boundary conditions. They compared the standard cylindrical cavity to conical and parabolic shapes and the simulation results showed that cavity and orifice height did not affect the maximum exit plane velocity appreciably for the three shapes. However, Feero et al. [11] presented experimental measurements for three axisymmetric synthetic jets with different cavity shapes to examine jet performance, while holding constant cavity volume, nozzle length and nozzle diameter. The experimental results showed that synthetic jet performance was dependent on cavity shape.

The Lattice Boltzmann method (LBM) offers an effective and efficient method to simulate complex fluid

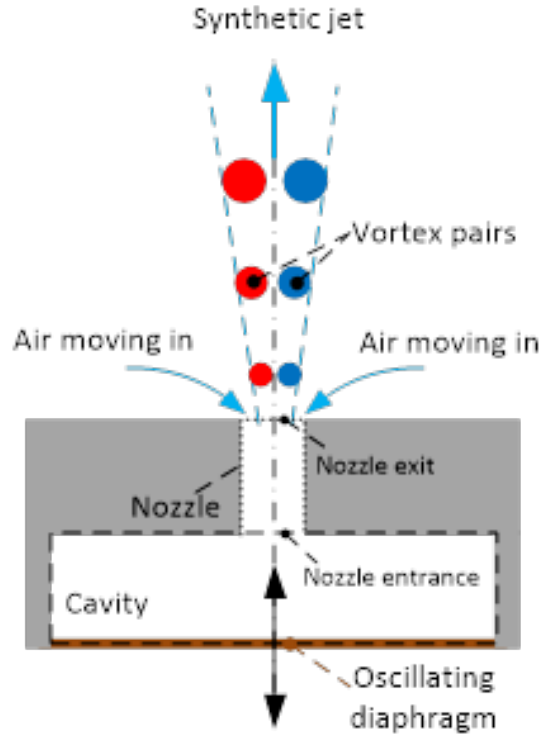


Figure 1.1: Schematic diagram of a synthetic jet actuator.

flow, allowing easy implementation of boundary conditions and can be used for unsteady flows, phase separation, evaporation, condensation, cavitation, solute and heat transport, buoyancy, and interactions with surfaces can readily be simulated. Instead of solving the classical macroscopic Navier-Stokes (N-S) equations, as is done with traditional CFD methods, LBM solves for a limited number of interactions with small particles to determine the exchange of momentum and energy by simulating streaming and collision processes [12]. The LBM is based on constructing simplified kinetic models containing the physics of microscopic and mesoscopic processes so that averaging can recover macroscopic properties that obeys the continuum equations [13].

LBM also has been applied in the study on flow control including flow separation control, mixing control, and turbulence control, using a pair of synthetic jets (SJs). Wang et al. [14] studied active control of wakes and one-dimensional vortex-induced vibrations (VIVs) from a single circular cylinder using a pair of synthetic jets (SJs) at a low Reynolds number $Re=100$ using a lattice Boltzmann method based numerical frame work. Using a hybrid approach of the lattice Boltzmann method for flow field computations and a finite-difference model, Mautner [15] studied the modified main channel flow results for various wall jet geometries (derived from synthetic jets), jet inlet conditions, scaling issues and Reynolds numbers. Fu et al. [16] reported on the use of the lattice Boltzmann method, in conjunction with Large-Eddy Simulations, to study an interesting phenomenon related to the suppression of vortex shedding from circular cylinders with high accuracy coupled with computational efficiency. It had been observed in experiments that vortex shedding and separated shear layer from a cylinder could be drastically reduced by the injection of a fluid jet into the approach flow.

The application of LBM for fluid flow simulations is far less common than, e.g., finite volume methods, however there is a significant body of findings in the literature that suggests that this method is more accurate and less computationally intensive compared to others. For this work, a 3-D simulation of synthetic jet cavities

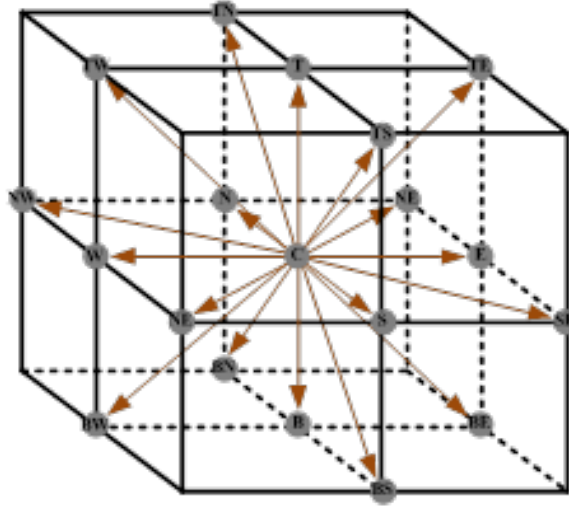


Figure 1.2: D3Q19 model for the 3-D LBM.

is conducted with the Lattice Boltzmann method. Based on the BGK model, the most popular model for the 3-D case, the D3Q19 model shown in Fig. 1.2, which consists of 19 distribution functions, was used [17]. GPU-based approaches [18] have been found to successfully accelerate solution by up to 10 times when compared to non-parallelized Lattice Boltzmann models. These approaches have been successfully implemented in urban flows [19] and rotational turbulence [20]

The goal of the present study is to investigate the influence of synthetic jets on cross-flows and, particularly, separated flow. 3-D non-dimensional numerical models of synthetic jet are employed to simulate this synthetic jet using the 3-D Lattice Boltzmann method. The performance of the synthetic jet will be evaluated in the context of flow control applications. Unsteady synthetic jet simulations are carried out, analyzed and compared.

Chapter 2

Numerical Method and Model

2.1 Lattice Boltzmann Model

The simulation in this study used the D3Q19 BGK collision model. To handle the complex geometry of the synthetic jet actuator, stationary lattices in the computational domain were generated from mesh voxelization of a 3D stereolithography model. The lower domain with stationary lattices were generated from the axis-aligned model of the synthetic jet actuator, then the external fluid domain and other boundary definitions are added to complete the domain definition (Fig. 2.1a).

There are multiple types of boundaries involved in the simulation, including fixed velocity inlet, outlet, moving wall (diaphragm) and bounce-back wall (solid/fluid interface) and are shown in Fig. 2.1b.

To improve numerical accuracy and simplify collision step processing, the half-way bounce-back method was implemented to process lattice nodes near the actuator wall. For half-way bounce-back, the no-slip wall is located at the middle of a grid, so the the distribution function reflects back to the opposite direction upon reaching the stationary nodes in the streaming step. The half-way bounce-back provides second order numerical approximation and impermeability for the stationary nodes, which means no special treatment is required to identify and process the surface nodes [21]. Both the fixed velocity inlet and the diaphragm were processed with a 3DQ19 equivalent of the Zou and He velocity boundary [21] before the collision step calculation. The unknown distribution functions were found from the existing distribution functions and the current velocity. Taking a node at the left boundary as an example, the unknown distribution functions in Fig. 2.3 are f_1, f_7, f_9, f_{15} and f_{17} . These

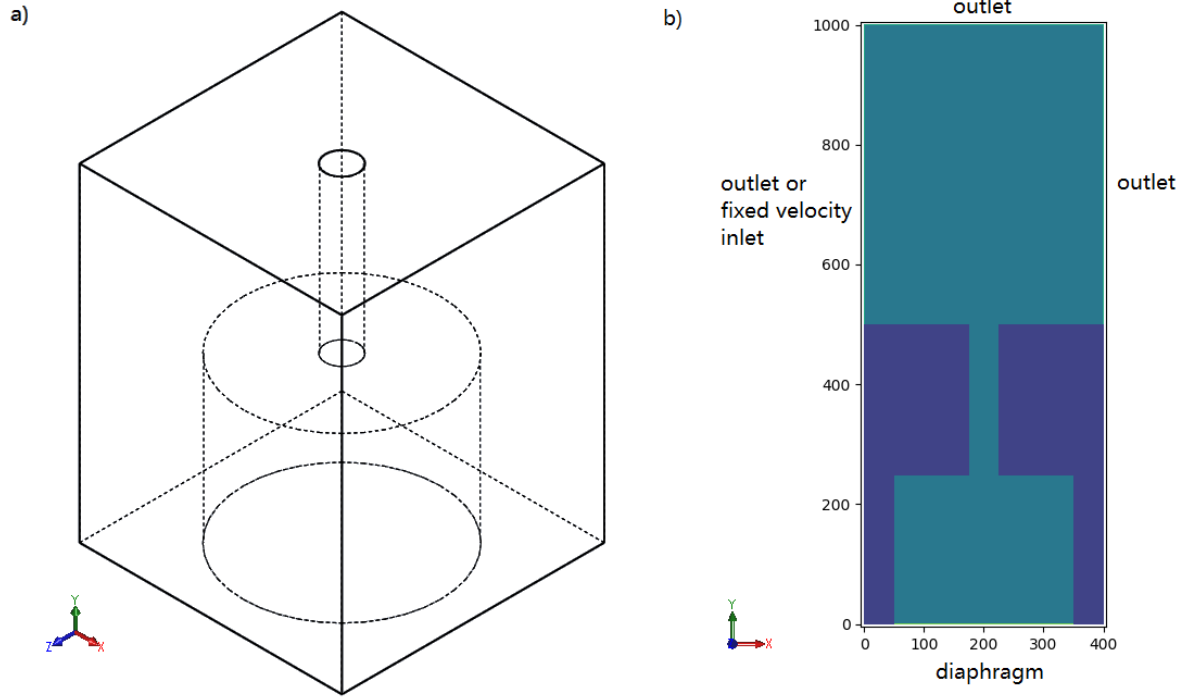


Figure 2.1: a) 3D model of synthetic jet actuator b) Middle plane of generated LBM domain along z axis.

unknowns are of the form [22]:

$$\begin{aligned}\rho &= [(f_0 + f_3 + f_4 + f_5 + f_6 + f_{11} + f_{12} + f_{13} + f_{14}) + \\ &\quad 2 \cdot (f_2 + f_8 + f_{10} + f_{16} + f_{18})] / (1 - u) \\ f_1 &= f_2 + \frac{1}{3} \rho u \\ f_7 &= f_8 + \frac{1}{6} \rho u + \frac{1}{2} \rho v - \frac{1}{2} (f_3 - f_4) - \frac{1}{2} (f_{11} - f_{12}) - \frac{1}{2} (f_{13} - f_{14}) \\ f_9 &= f_{10} + \frac{1}{6} \rho u - \frac{1}{2} \rho v + \frac{1}{2} (f_3 - f_4) + \frac{1}{2} (f_{11} - f_{12}) + \frac{1}{2} (f_{13} - f_{14}) \\ f_{15} &= f_{16} + \frac{1}{6} \rho u + \frac{1}{2} \rho w - \frac{1}{2} (f_5 - f_6) - \frac{1}{2} (f_{11} - f_{12}) + \frac{1}{2} (f_{13} - f_{14}) \\ f_{17} &= f_{18} + \frac{1}{6} \rho u - \frac{1}{2} \rho w + \frac{1}{2} (f_5 - f_6) + \frac{1}{2} (f_{11} - f_{12}) - \frac{1}{2} (f_{13} - f_{14})\end{aligned}$$

For the outlet nodes with unknown macroscopic properties, the unknown distribution functions were obtained from extrapolation of the nearest nodes. Here, the unknowns were acquired from linear extrapolation in the outward normal direction:

$$f_{i,n} = 2f_{i,n-1} + 2f_{i,n-2}$$

where i is the index of unknowns, and n is the position of boundary node in outward normal direction.

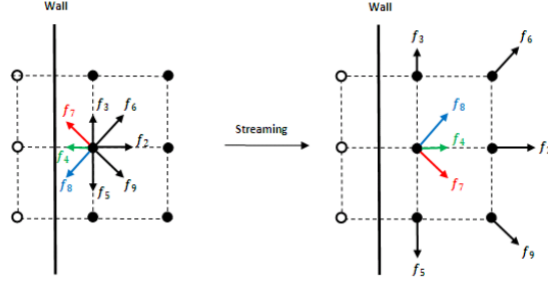


Figure 2.2: Illustration of half-way bounce-back.

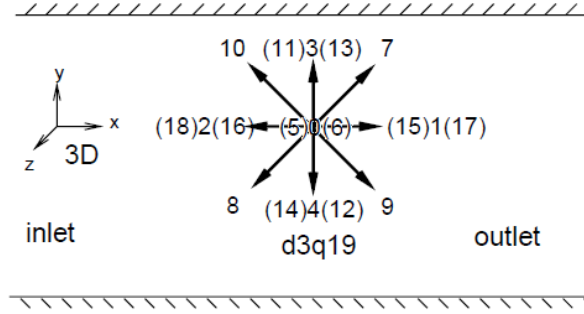


Figure 2.3: D3Q19 in xy plane (distribution functions labelled from z+ to z-).

2.2 GPU implementation

The GPU computation of the BGK model used the Numba CUDA compiler with Nvidia GPUs. To perform the D3Q19 model, an array of size $N_x \times N_y \times N_z \times 19$ is allocated to store the particle distribution functions. N_x , N_y and N_z are the number of lattice nodes in the x-, y- and z- axes of the lattice domain respectively, while the last dimension is used to store the 19 distribution functions in the corresponding node.

The distribution functions f_1, f_2, \dots, f_{18} of stationary nodes are initialized to 0, whereas those of the fluid nodes are initialized to the lattice weights of D3Q19. For the D3Q19 model, the lattice weights are

$$w_i = \begin{cases} 1/3, & \text{if } i = 0 \\ 1/18, & i=1,2,\dots,6 \\ 1/36, & i=7,8,\dots,18 \end{cases}$$

The work flow for the simulation is presented in Fig. 2.4 and shows where GPU processing is implemented. The cycle begins with an array holding the distribution functions at time t . Then, macroscopic variables such as velocities and pressure can be extracted from planes of interest to generate data file output. GPU processing starts after data extraction to calculate the distribution functions for the next time step at $t + \Delta t$. Finally, a new cycle begins after time update and data output. To process data with GPU, the data have to be transferred into the device memory of the GPU from the host memory. For an array allocated above with size of $1000 \times 500 \times 500 \times 19$ and 32 bit floating point number for each element, this requires 17.69GB. The device memory limits the transfer of

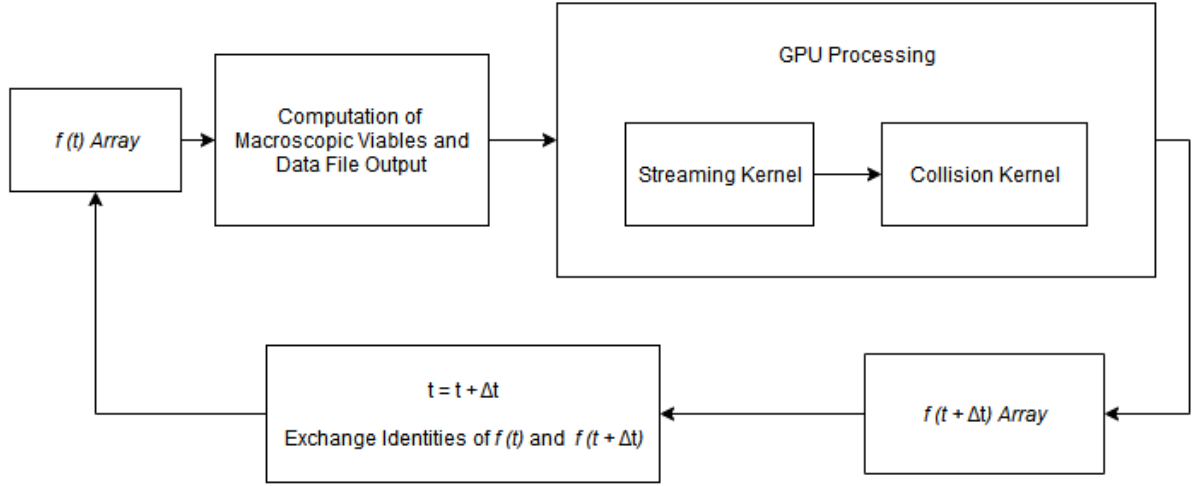


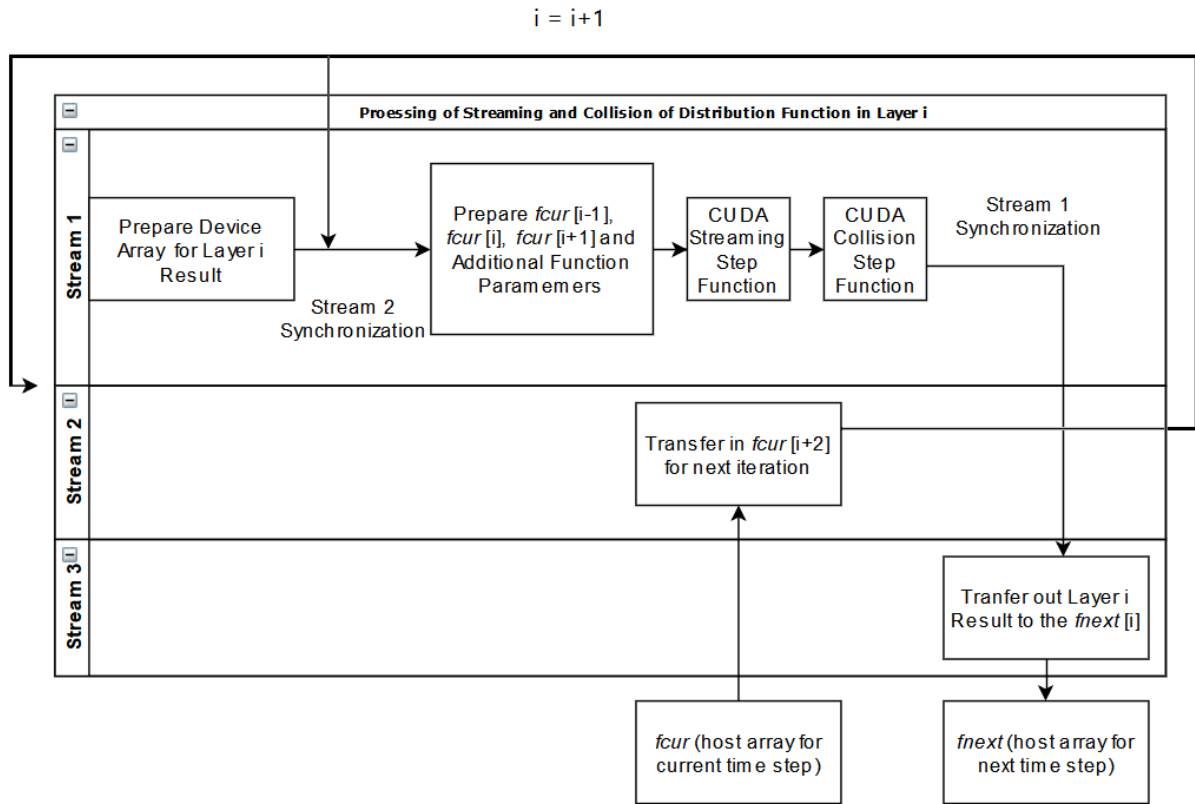
Figure 2.4: Work flow cycle of LBM simulation

the entire distribution function array because of its size, and the transfer-in and transfer-out of the entire array would have a heavy time cost between actual GPU computation kernel steps. Therefore, it is a good practice to dissect the array into a number of layers along an axis and manually handle the data transfer for the entire array.

In this study, three asynchronous streams of commands are applied in the GPU processing to reduce the time cost by overlapping data transfer and computation [23]. Stream 1 is implemented to execute CUDA kernels for streaming and collision of distribution functions in the current layer. Stream 2 is assigned to transfer data needed for the computation of the next layer during the execution of CUDA kernels, while Stream 3 transfers computation result of the current layer computation back to the host memory. In addition, host synchronization checkpoints await commands in the stream to finish to properly sequence them, so no race condition shall happen. Fig. 2.5 shows the detailed steps involved in the synchronization of CUDA streams.

CUDA is a parallel computing platform developed by Nvidia to enable programmers to execute GPU instruction sets on Nvidia GPU for General Purpose Processing, allowing execution of a large number of parallel threads on the GPU stream processors. Because of the multicore architecture and throughput optimization, GPUs are suitable for high density parallel processing tasks like the streaming step and collision step for each lattice node, and they could be $100\times$ faster than their CPU counterparts.

The layer decomposition described above reduces the problem from 3D parallel processing of an entire array to 2D parallel processing of each layer. Because of the streaming of distribution functions from neighbouring nodes, its processing requires data from the current layer, the layer below and the layer above. In addition, the post streaming distribution function has to be stored in a separate output layer to avoid conflict with processing of next layer. The collision step kernel is much simpler, since it does not affect neighbouring nodes. Therefore, only the output layer from the streaming kernel is required as array input, and the post collision distributions could be stored back to the input array. Moreover, distribution functions on the boundary could also be updated in the collision kernel before the actual collision to realize fixed velocity inlet and moving wall.

Figure 2.5: Arrangement of CUDA stream of commands for layer i .

Chapter 3

Computational Domain

To study the influence of the SJA on a cross-flow, two 3D LBM computational domains were created. Fig. 3.1 shows the geometries of these domains where there was (a) flat plate flow over the SJA and (b) a 16° incline of the surface that allowed a separated flow over the SJA. The blue region is the wall of the nozzle and the fixed velocity inlet, diaphragm and outlet are marked with orange, red and green respectively.

Dimensions are normalized by the nozzle diameter d , where $d = 2\text{mm}$. The size of the entire computational domain is $32\text{mm} \times 40\text{mm} \times 16\text{mm}$ or $16d \times 20d \times 8d$. Flow enters from the left and moves to the right with a fixed velocity and the diaphragm oscillates in the y -direction at constant frequency. To meet the formation criteria for a synthetic jet actuator, the physical conditions, which include maximum physical velocity of diaphragm $U_{dia-pmax}$, diaphragm oscillation frequency f , the fixed cross flow inlet velocity $U_{inlet-p}$ and kinematic viscosity ν , were set to 0.5m/s , 300Hz , 6m/s and $6.89 \times 10^{-5}\text{m}^2/\text{s}$ respectively, which lead to a study case with Stokes number $S = 11$ and $Re_{\overline{U}} = 141$.

In addition, the maximum diaphragm velocity in LB unit, $U_{dia-LBmax}$, was set to $0.006u$. Thus, with the lattice scale domain of size $800 \times 1000 \times 400$, the other LBM parameters required could be obtained as follow.

1. Lattice unit length, $\Delta x = l/N_x = 0.04\text{mm}$
2. Time step, $\Delta t = \Delta x \cdot U_{dia-LBmax} / U_{dia-pmax} = 4.8 \times 10^{-7}\text{s}$
3. Fixed cross flow velocity in LB unit, $U_{inlet-LB} = U_{inlet-p} / (\Delta x / \Delta t) = 0.072u$
4. Diaphragm velocity in LB unit, $U_{dia-LB} = U_{dia-LBmax} \sin(2\pi f \cdot (t))$
5. Viscosity in LB unit, $Nu_{LB} = \nu / (\Delta x^2 / \Delta t) = 0.02067$



Chapter 4

Results and Discussions

4.1 GPU performance

The LBM was performed on the Southern Ontario Smart Computing Innovation Platform GPU cluster node. With $4 \times$ NVIDIA Tesla P100 GPUs (16GB) per node, the GPU cluster node was capable of processing 12.5ms (26042 time steps) in 24 hours on average, which means 3.32s per time step. Given the distribution array with size of 17.69GB, the throughput could reach 5.32GB/s for the D3Q19 BGK collision model. The computational cost per time step is comparable to that of a CPU based 2DQ9 LBM simulation for the same problem. Thus, greater than $100 \times$ acceleration was achieved using the GPU.

4.2 Flow from nozzle

Fig. 4.1 is the mean axial velocity ($y+$ direction) in the nozzle exit plane and the axial velocity of diaphragm recorded in the simulation.

The diaphragm flux and nozzle exit flux are sinusoidal throughout the cycle. The phase delay of the exit flux approaches 180° as expected (Mu et al. [24]). In the 3rd diaphragm working cycle from 8.333ms to 11.667ms, the phase angle θ from 0° to 180° roughly matching the ingestion stroke at the nozzle exit and from 180° to 360° corresponds to expulsion stroke. The subsequent flow discussions will be centered around the 3rd diaphragm working cycle.

From Fig. 4.1 b, $\theta = 68^\circ$ corresponds to maximum ingestion magnitude (phase angle $\phi = 270^\circ$ at $y = 8d$), while $\theta = 264^\circ$ corresponds to maximum expulsion magnitude (phase angle $\phi = 90^\circ$ at $y = 8d$). The axial velocity profile at the exit plane is presented in Fig. 4.2. To minimize the influence of cross flow entrainment, the profile was taken at $y = 8d$ from the bottom. The centerline velocity at maximum expulsion (3.69 m/s) is slightly higher than the centerline velocity at maximum ingestion (2.99 m/s). As seen by Mu et al. [24] and Ziade et al. [25], in comparison to the maximum expulsion, there is more flux entering from the periphery of the nozzle at maximum ingestion. The flow profile in the circular duct can be characterized by the Stokes number S . For $S > 2$, the spatially averaged velocity should be greater than 50% of the centerline velocity. As S approaches 20 the spatially averaged velocity should reach 90% of the centerline velocity. With $S = 11$ in this study case, the velocity profile has shown agreement with the theory.

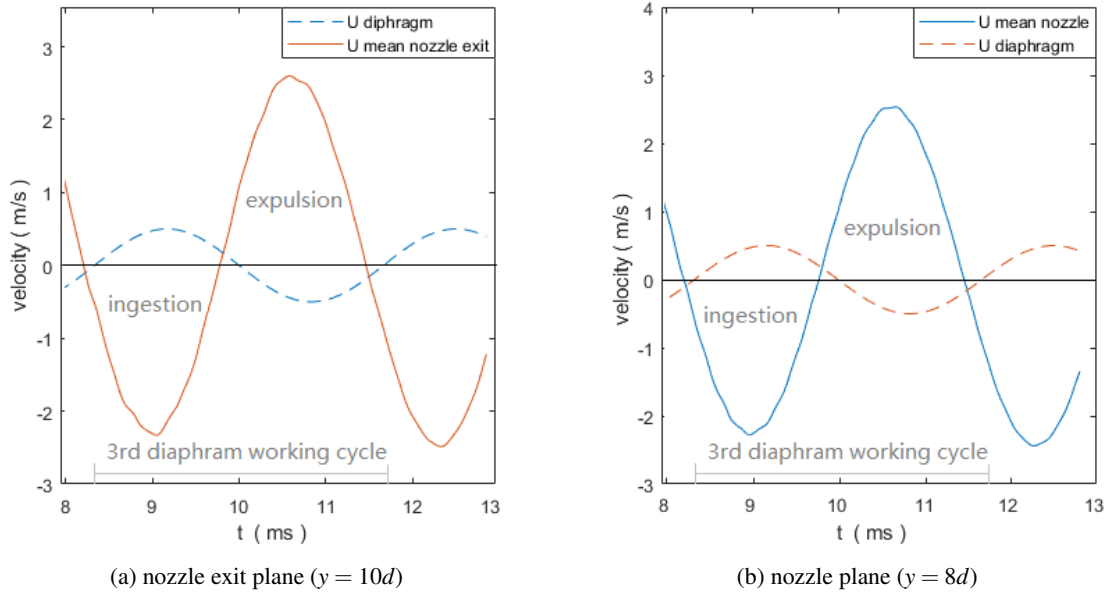
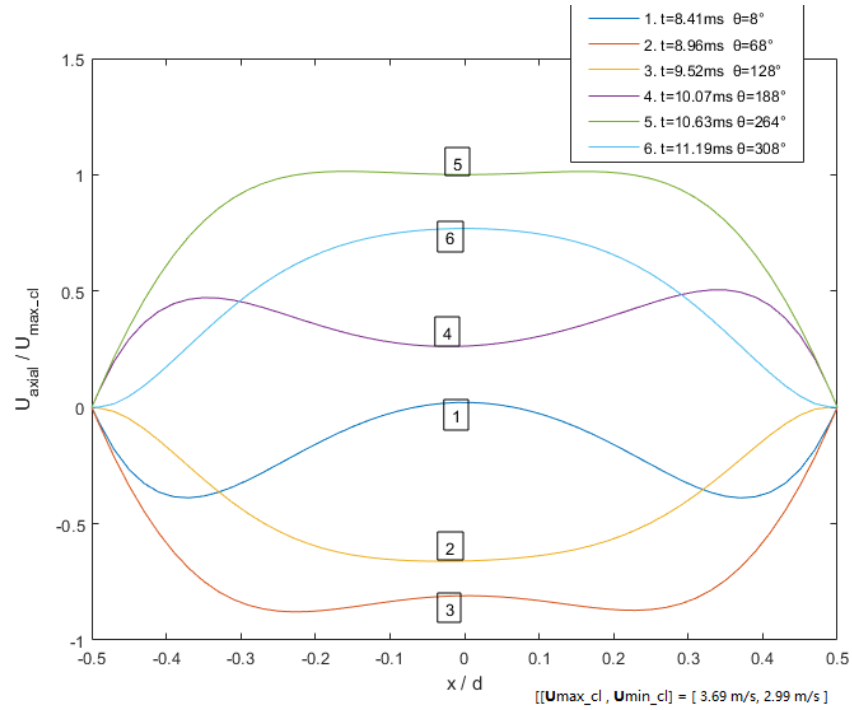
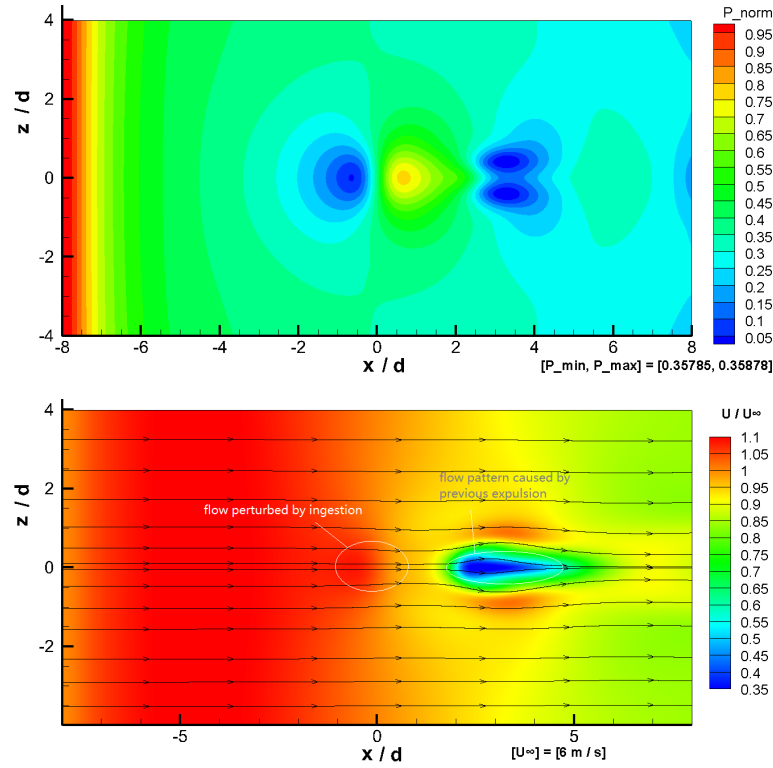


Figure 4.1: Mean jet velocity of the nozzle planes versus time

Figure 4.2: Axial jet velocity profile along the exit line at $y = 8d$

(a) Pressure and velocity profiles of ingestion stroke $\theta = 84^\circ$

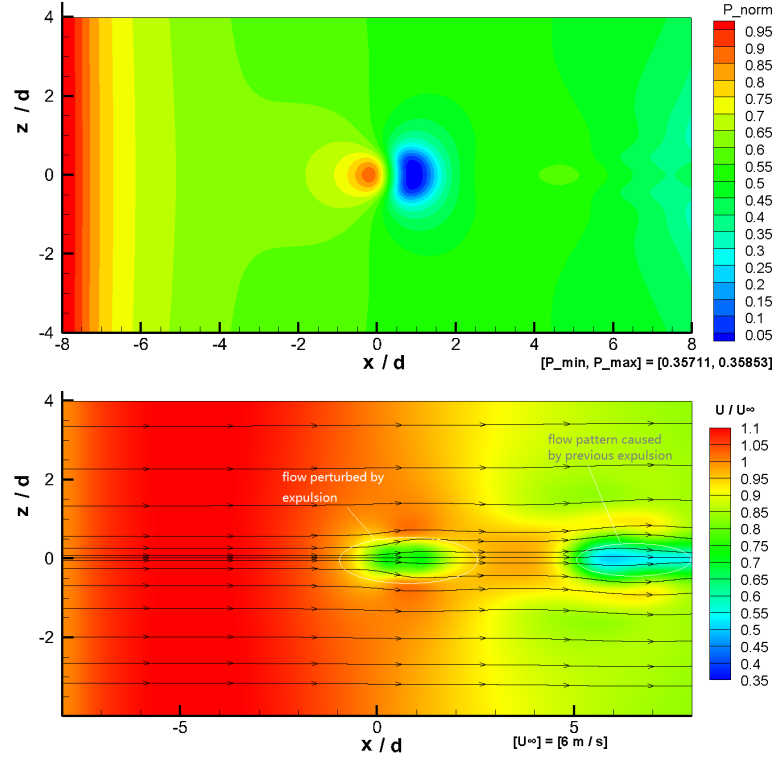
4.3 Flow development in x-z plane

Fig. 4.3 shows the top-down view of the pressure contour plots and velocity profiles at $y = 10.6d$ from the bottom, where the axial origin is defined at the nozzle center. The pressure values in Fig. 4.3 are normalized by the maximum and minimum dimensionless LB pressures in the plot frame, such that $P_{norm} = (P - P_{min}) / (P_{max} - P_{min})$. The velocities are normalized by the free stream velocity U_∞ , where $U_\infty = 6 \text{ m/s}$. Due to the cross flow in the $x+$ direction and the increased boundary layer thickness, the pressure contour plot shows a general trend of negative pressure gradient in $x+$ direction, while the velocity contour plot shows decrease in velocity magnitude overall.

At the peak of ingestion stroke (Fig. 4.3a), the synthetic jet exits from nozzle and perturbs the cross flow. On the pressure contour plot, the jet flow is localized at the pressure center pair ($x = 0d$), which includes a low pressure center at the front and a high pressure center at the back. In the velocity profile, the streamlines converge at the low pressure center, and then diverge at the high pressure center. Behind the pressure center pair, there is a low pressure region which corresponds to flow induction created by the previous expulsion stroke on the velocity profile.

At the peak of expulsion stroke (Fig. 4.3b), the order of pressure center pair is opposite to that of the ingestion stroke with a leading high pressure center and a following low pressure center. The flow pattern is also opposite to the flow pattern in the ingestion stroke, with divergence at the front and convergence at the back.

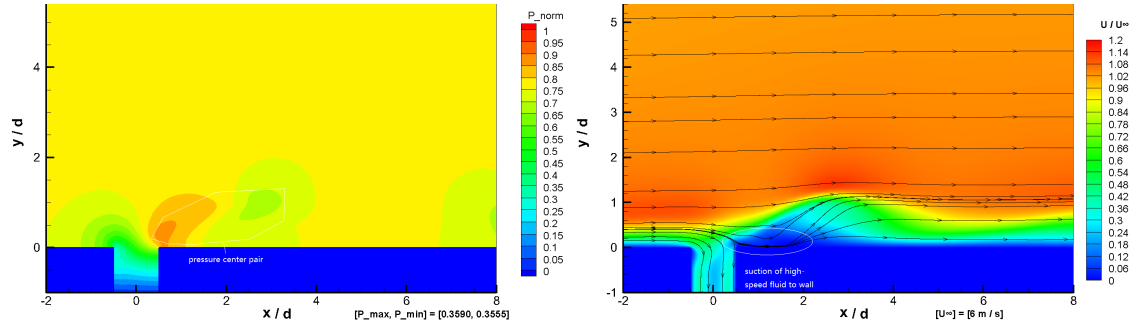
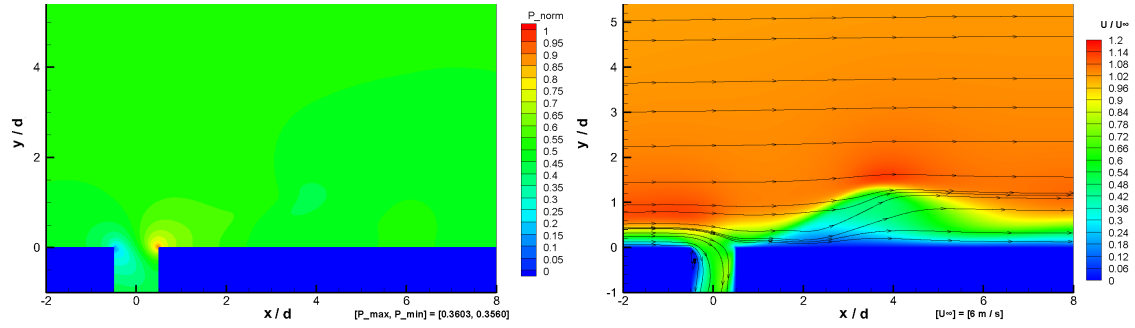
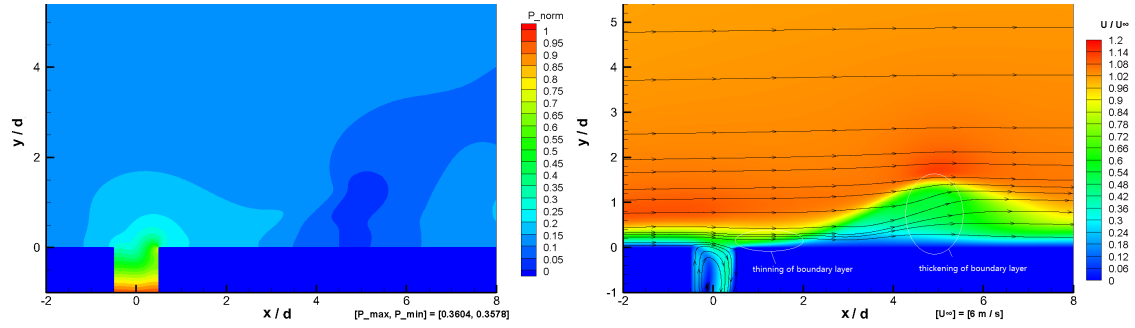
Overall, both during ingestion and expulsion the influence of the SJA is limited to a small region roughly $1d$ wide. This suggests a limited geometric range of effective control and has been seen by others [26].

(b) Pressure and velocity profiles of expulsion stroke $\theta = 270^\circ$ Figure 4.3: pressure contour plots and velocity contour plots with streamlines in x - z plane at $y = 10.6d$ from bottom

4.4 Flow development in x - y plane

For flow over the flat plate, with the top plate boundary parallel to the cross-flow (Fig. 3.1a, the flow within the cavity is similar to that seen by Mu et al. [24] and Ziade et al. [25]. Fig. 4.4 shows the pressure contour plots and velocity profiles of the external region obtained in the middle section shown in red in Fig. 3.1. Fig. 4.4 a–c correspond to the ingestion stroke of the cycle, while Fig. 4.4 d–f are the expulsion stroke of the cycle.

During expulsion, as the jet exited the nozzle, it bends in the direction of the cross-flow and moves downstream (Fig. 4.4d). This acts to energize and thicken the local boundary layer and leads to a negative pressure gradient above the nozzle exit, which is shown in the pressure contour plot as a pressure center pair with a high pressure center at the front and a low pressure center at the back. This pressure center pair moves up as fluid is pushed out. At the height of expulsion $\theta = 270^\circ$ (Fig. 4.4e), the presence of low pressure center leads to adverse pressure gradient downstream and reversed flow downstream near the wall. Then, this pressure center pair shifts downstream of the nozzle exit as the jet transitions to the ingestion portion of the cycle from $\theta = 330^\circ$ to $\theta = 30^\circ$ (Fig. 4.4 f–a), which allows the suction of high-speed outer fluid toward the wall at the beginning of the ingestion stroke. On the other hand, low-speed fluid in the flow upstream is also continuously sucked into the nozzle during the ingestion stroke, which leads to significant thinning of boundary layer downstream (Fig. 4.4 b–c). It is noted that these features would not be captured with a periodic boundary condition (e.g., a velocity boundary at the wall).

(a) Ingestion stroke $\theta = 30^\circ$ (b) Ingestion stroke $\theta = 90^\circ$ (c) Ingestion stroke $\theta = 150^\circ$

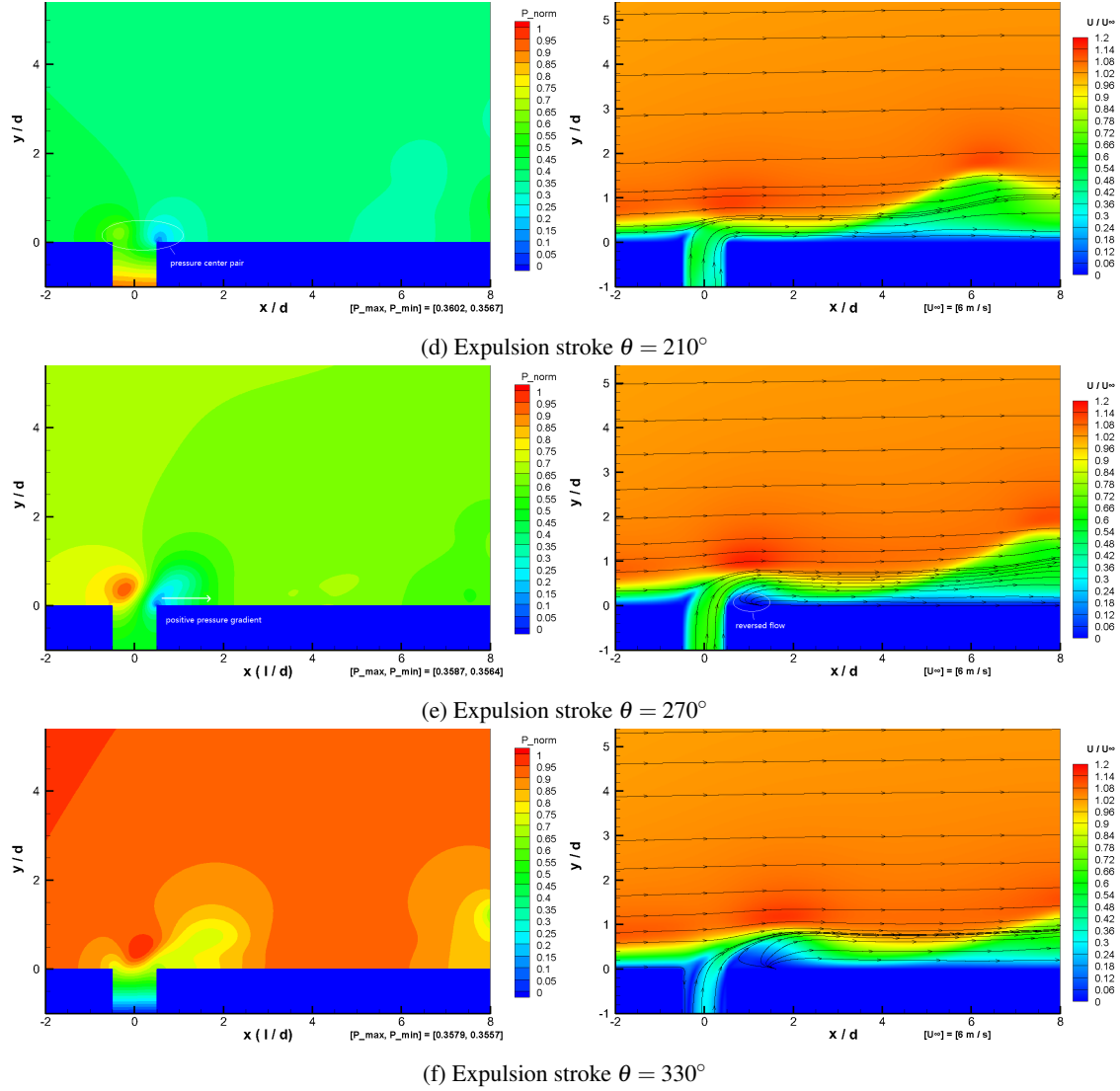


Figure 4.4: Pressure and velocity profiles in x-y plane (flat plate flow)

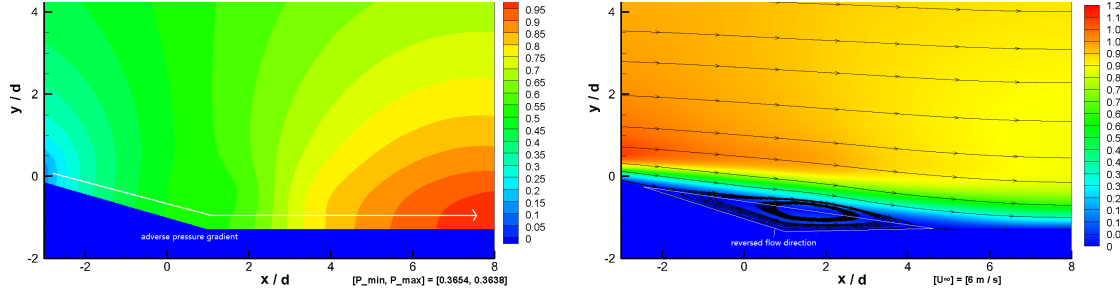


Figure 4.5: Pressure and velocity profiles in x - y plane (separated flow without SJA, $t = 10.83$ ms)

4.5 Separated flow

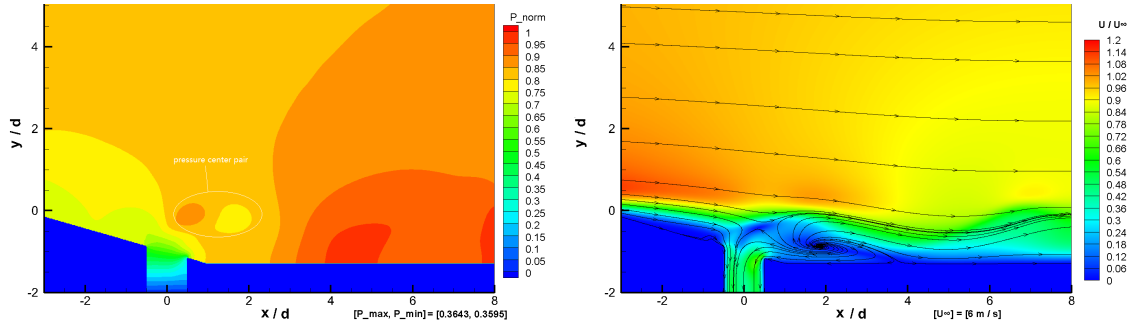
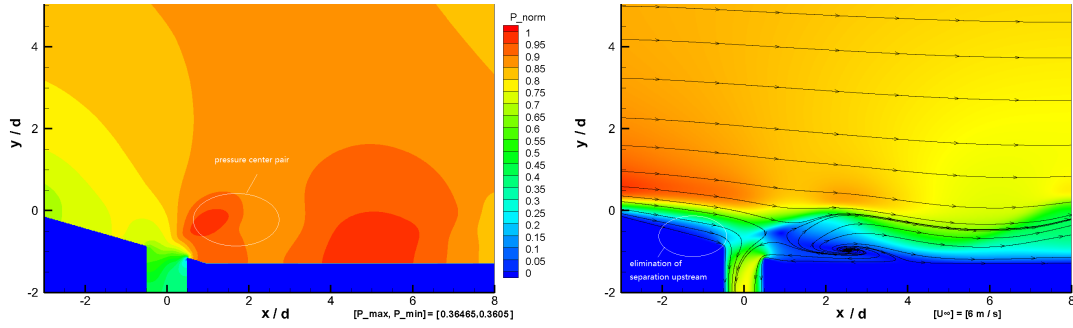
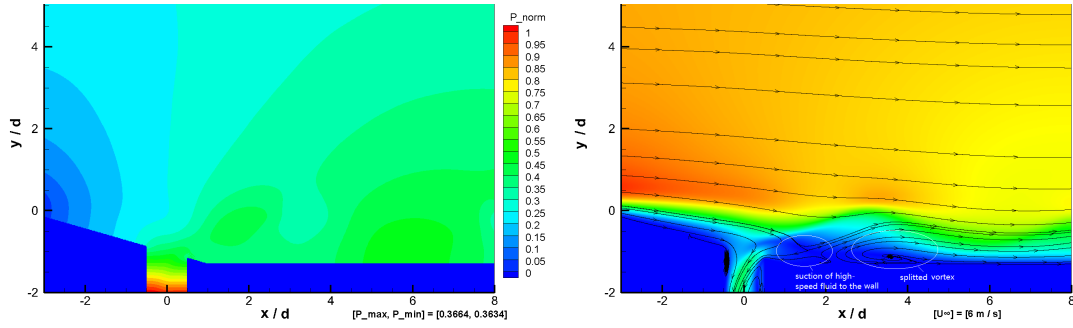
To study the influence of SJA on a separated flow, flow separation without an SJA was modeled and simulated first. The domain geometry was close to Fig. 3.1b but without the nozzle and cavity.

By introducing a slope of 16° at the domain entrance, an adverse pressure gradient is formed along the slope as shown in Fig. 4.5. This leads to rapid deceleration of flow, and reversed flow direction close to the boundary. As expansion is returned to horizontal flow, the cross flow reattaches to the wall and forms an enclosed separation vortex. At time $t = 10.83$ ms (corresponding to the 3^{rd} diaphragm cycle of the SJA), the cross flow separates at $x = -2d$ then reattaches at $x = 4.5d$. For the next stage of the work, the center of nozzle exit is positioned at $x = 0$ for the controlled cases.

By introducing the SJA at the $x = 0$ position (Fig. 4.6), the SJA directs high-speed fluid toward the wall. For the pressure, the immediate effect of the SJA is a pressure peak over the nozzle exit that induces flow downstream that acts to minimize flow separation. While slightly downstream of the separation point, the position of the SJA is within the range studied by Feero et al. [2]

At the beginning of the expulsion stroke ($\theta = 264^\circ$ Fig. 4.6d), a pressure center pair similar to the one in the flat plate flow case could be found above the nozzle, while another pressure center pair could be found downstream which is from the previous expulsion ingestion cycle. This former bends flow from the nozzle exit, while the latter leads to the suction of high-speed fluid to the wall downstream, which corresponds to the early reattachment point at $x = 2.5d$ in the velocity profile. From $\theta = 198^\circ$ to $\theta = 318^\circ$ (Fig. 4.6 d-f), the separation vortex expands laterally in the $x+$ direction as the downstream pressure center pair moves with the cross flow until the ingestion stroke begins. In the ingestion stroke, the pressure pair near the nozzle drives the outer high-speed fluid to the wall in the same way as the one in the flat plate flow case. This lead to the suppression and splitting of the separation vortex downstream as shown in Fig. 4.6c, when combined with the suction of the low-speed fluid near the nozzle exit. In addition, the nozzle suction also completely eliminates the reverse flow upstream.

Overall, as compared to the reference case without the SJA, the case with the SJA shows significant suppression of fluid separation during both the expulsion stroke and the ingestion stroke. The suppression effect is most significant at the end of ingestion stroke (Fig. 4.6c), as the nozzle suction dominates both the upstream boundary layer and the downstream boundary layer.

(a) Ingestion stroke $\theta = 18^\circ$ (b) Ingestion stroke $\theta = 78^\circ$ (c) Ingestion stroke $\theta = 138^\circ$

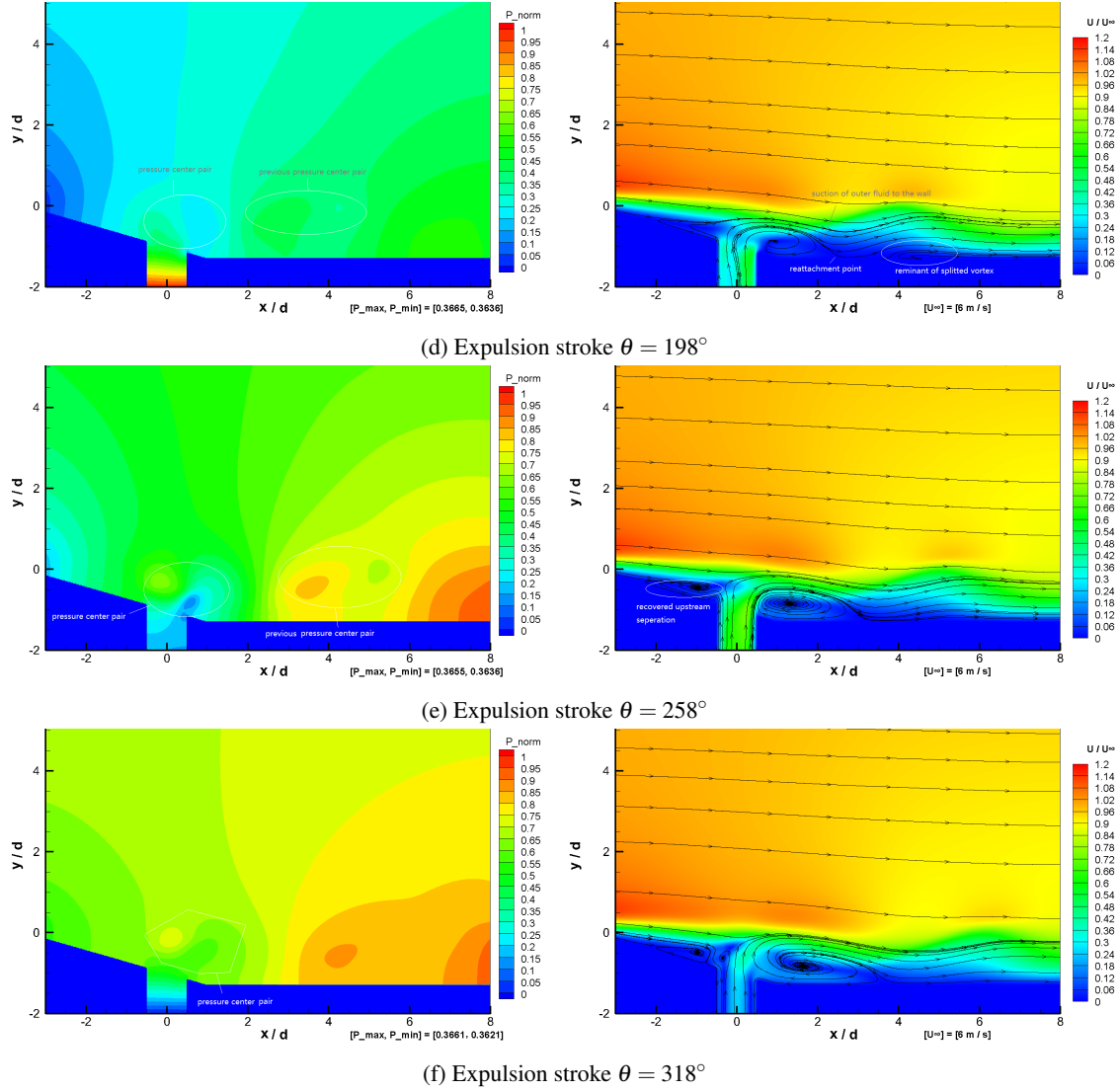


Figure 4.6: Pressure and velocity profiles in x-y plane (separated flow)

Chapter 5

Conclusions

A GPU based Lattice–Boltzmann method was applied to study the influence of a synthetic jet locally on a separated flow. LBM was useful in allowing a smaller computational domain while retaining a good description of the flow. Using the GPU, it was possible to study fine–scale motion with an increased number of lattice units. The introduction of the SJA showed an alternating pressure gradient during operation. This resulted in drawing high–momentum fluid toward the wall and assisted in forcing flow reattachment. The small spatial influence of the SJA in operation suggests the need for array based control with small separation between SJAs. However, the flow disturbances do clearly have long lifetimes in the flow.

Bibliography

- [1] D. Greenblatt, K.B. Paschal, Y. Chung-Sheng, J. Harris, *AIAA Journal* **44**(12), 2831 (2006). DOI 10.2514/1.19324. URL <http://arc.aiaa.org/doi/10.2514/1.19324>
- [2] M.A. Feero, P. Lavoie, P.E. Sullivan, *Experiments in Fluids* **58**(8), 99 (2017). DOI 10.1007/s00348-017-2387-x. URL <http://link.springer.com/10.1007/s00348-017-2387-x>
- [3] A. Pavlova, M. Amitay, *Journal of Heat Transfer* **128**(9), 897 (2006). DOI 10.1115/1.2241889. URL <http://heattransfer.asmedigitalcollection.asme.org/article.aspx?articleid=1448464>
- [4] D.S. Kercher, J.B. Lee, O. Brand, M.G. Allen, A. Glezer, *IEEE Transactions on Components and Packaging Technologies* **26**(2), 359 (2003). DOI 10.1109/TCAPT.2003.815116
- [5] A. Glezer, M. Amitay, *Annual Review of Fluid Mechanics* **34**, 503 (2002). DOI 10.1146/annurev.fluid.34.090501.094913
- [6] C. Lee, G. Hong, Q.P. Ha, S.G. Mallinson, in *Sensors and Actuators, A: Physical*, vol. 108 (2003), vol. 108, pp. 168–174. DOI 10.1016/S0924-4247(03)00267-X
- [7] X. Ma, H. Guo, Z. Fan, L. Zhang, in *Procedia Engineering*, vol. 31 (2012), vol. 31, pp. 416–421. DOI 10.1016/j.proeng.2012.01.1045
- [8] U.S. Bhapkar, A. Srivastava, A. Agrawal, *Experimental Thermal and Fluid Science* **68**, 392 (2015). DOI 10.1016/j.expthermflusci.2015.05.006
- [9] Y. Utturkar, R. Mittal, P. Rampunggoon, L. Cattafesta, in *40th AIAA Aerospace Sciences Meeting & Exhibit* (Reno, NV, United States, 2002), pp. 2002–0124. DOI 10.2514/6.2002-124. URL <http://arc.aiaa.org/doi/abs/10.2514/6.2002-124>
- [10] M. Jain, B. Puranik, A. Agrawal, *Sensors and Actuators A: Physical* **165**(2), 351 (2011). DOI 10.1016/j.sna.2010.11.001. URL <http://www.sciencedirect.com/science/article/pii/S092442471000484X>
- [11] M.A. Feero, P. Lavoie, P.E. Sullivan, *Sensors and Actuators A:Physical* **223**, 1 (2015). DOI 10.1016/j.sna.2014.12.004. URL <http://www.sciencedirect.com/science/article/pii/S092442471400510X>
- [12] D. Perumal, A.K. Dass, *CFD Letters* **2**(1), 25 (2010)
- [13] D. Perumal, A.K. Dass, *Computers & Mathematics with Applications* **61**(12), 3711 (2011). DOI 10.1016/j.camwa.2010.03.053
- [14] C. Wang, H. Tang, F. Duan, S.C. Yu, *Journal of Fluids and Structures* **60**, 160 (2016). DOI 10.1016/j.jfluidstructs.2015.11.003

- [15] T. Mautner, *Biosensors & Bioelectronics* **19**(11), 1409 (2004). DOI 10.1016/j.bios.2003.12.023
- [16] G. Fu, B.A. Younis, L. Sun, S. Dai, in *ASME 2016 35th International Conference on Ocean, Offshore and Arctic Engineering* (American Society of Mechanical Engineers, 2016), pp. V002T08A071–V002T08A071
- [17] K. Iglberger, N. Thürey, U. Rüdè, *Computers and Mathematics with Applications* **55**(7), 1461 (2008). DOI 10.1016/j.camwa.2007.08.022
- [18] N. Delbosc, J.L. Summers, A.I. Khan, N. Kapur, C.J. Noakes, *Computers and Mathematics with Applications* **67**(2), 462 (2014). DOI 10.1016/j.camwa.2013.10.002
- [19] M.F. King, A. Khan, N. Delbosc, H.L. Gough, C. Halios, J.F. Barlow, C.J. Noakes, *Building and Environment* **125**, 273 (2017). DOI 10.1016/j.buildenv.2017.08.048
- [20] H. Yu, R. Chen, H. Wang, Z. Yuan, Y. Zhao, Y. An, Y. Xu, L. Zhu, *Computers and Mathematics with Applications* **67**(2), 445 (2014). DOI 10.1016/j.camwa.2013.09.017
- [21] Q. Zou, X. He, *Physics of Fluids* **9**(6), 1591 (1997). DOI 10.1063/1.869307. URL <http://aip.scitation.org/doi/10.1063/1.869307>
- [22] C.F. Ho, C. Chang, K.H. Lin, C.A. Lin, *CMES - Computer Modeling in Engineering and Sciences* **44**, 137 (2009). DOI 10.3970/cmes.2009.044.137. URL <https://www.techscience.com/doi/10.3970/cmes.2009.044.137.pdf>
- [23] T. Ben-Nun, M. Sutton, S. Pai, K. Pingali, *ACM SIGPLAN Notices* **52**(8), 235 (2017). DOI 10.1145/3155284.3018756. URL <http://doi.acm.org/10.1145/3155284.3018756>
- [24] H. Mu, Q. Yan, W. Wei, P.E. Sullivan, *AIAA Journal* **56**(6), 2499 (2018). DOI 10.2514/1.J056921
- [25] P. Ziadé, M.A. Feero, P.E. Sullivan, *International Journal of Heat and Fluid Flow* **74**, 187 (2018). DOI 10.1016/j.ijheatfluidflow.2018.10.001. URL <https://www.sciencedirect.com/science/article/pii/S0142727X18305770>
- [26] M.A. Feero, P. Lavoie, P.E. Sullivan, *Journal of Visualization* **20**(1), 45 (2017). DOI 10.1007/s12650-016-0365-7. URL <http://link.springer.com/10.1007/s12650-016-0365-7>